An efficient semi-implicit compressible solver for large-eddy simulations

By V. Moureau, C. Bérat† AND H. Pitsch

1. Motivation and objectives

In most combustion devices, the Mach number is small, and the most efficient computational approach is the solving of the low-Mach number formulation of the Navier-Stokes equations. In this approach, the acoustic waves propagate at an infinite speed. Nevertheless, when the acoustic speed plays an important role, as in the formation of instabilities, the compressible Navier-Stokes equations must be solved. If these equations are solved explicitly, the acoustic CFL condition imposes a drastic limit on the time-step for flows of low convective CFL number. Then, a semi-implicit approach, in which acoustic waves are solved implicitly, potentially offers significant efficiency gains using larger time-steps.

Implicit compressible solvers able to deal with low-Mach number flows fall into two basic categories. The first category consists of the density-based solvers, which are originally designed for high-Mach number flows. When the Mach number goes to zero, the algebraic system of these solvers becomes ill-conditioned (Turkel *et al.* 1997; Guillard & Viozat 1998). This issue is classically overcome by using preconditioning techniques (Turkel 1987) or by performing a Taylor-series expansion in Mach number (Choi & Merkle 1993). The second category is that of the pressure-based solvers. These solvers were originally developed for incompressible flows. In this case, the pressure gradient in the momentum equation acts as a source term needed to maintain the incompressibility constraint. This dynamic pressure comes from the solution of a Poisson equation. Using this type of approach ensures that in contrast to non-preconditioned density-based systems, the pressure variations remain finite in the low-Mach limit. Many pressure-based implicit compressible solvers have been designed since the pioneering work of Harlow & Amsden (1968). Unfortunately, these methods are either first-order in time (Karki & Patankar 1989), non-mass conservative (Yoon & Yabe 1999), or they necessitate a very costly inner loop to couple the energy (or enthalpy) equation to the other equations (Zienkiewicz *et al.* 1999; Wall *et al.* 2002).

A suitable method for the computation of acoustic instabilities in a combustion device needs to be mass conservative and efficient, which precludes the use of an inner loop to converge the energy equation, and it has to have low-dissipation. In this paper, a method that fulfills these requirements is proposed. It is a fractional-step method (Kim & Moin 1985) based on a characteristic splitting. This method consists of an advection and a pressure-correction step. In the pressure-correction step, a Helmholtz equation is solved implicitly to remove the acoustic CFL condition. The characteristic splitting allows the decoupling of the acoustic waves from the advection, and a second-order spatial and temporal convergence for linear acoustics can be obtained without inner loop. When this method is used in combination with a kinetic-energy conserving scheme for the advection

† Turboméca - Safran Group, 64522 Bordes, France

step (Mahesh *et al.* 2004), the method is kinetic-energy conserving in the incompressible limit.

The proposed method is verified by performing simple test cases. The first test is a linear-acoustic wave propagation, the second test is a low-Mach vortex advection, and the third test consists of the computation of an under-resolved Homogeneous Isotropic Turbulence (HIT) case at an infinite Reynolds number. These tests are performed to demonstrate all the properties mentioned above. Finally, the new compressible solver is applied in an LES computation of the cold flow of an industrial lean-premixed burner. This computation has also been performed with an incompressible solver with the same mean convective CFL and the same spatial and temporal schemes. It will be demonstrated that the computational time required for the fully compressible simulation is only slightly higher than when using a low-Mach number solver.

2. A characteristic-based fractional-step method

In this section, the characteristic splitting of the Navier-Stokes equations is described first. Then, the full algorithm of the new compressible solver is presented and analyzed for linear acoustics and for the low-Mach limit.

2.1. *Compressible large-eddy simulation equations*

The compressible Navier-Stokes equations for the large-eddy simulation of a non-reactive flow are:

$$\frac{\partial \bar{\rho}}{\partial t} + \nabla \cdot (\bar{\rho}\tilde{\mathbf{u}}) = 0 \tag{2.1}$$

$$\frac{\partial \bar{\rho}\tilde{\mathbf{u}}}{\partial t} + \nabla \cdot (\bar{\rho}\tilde{\mathbf{u}}\tilde{\mathbf{u}}) = -\nabla \bar{P} + \nabla \cdot \mathbf{t} \tag{2.2}$$

$$\frac{\partial \bar{\rho}\tilde{h}}{\partial t} + \nabla \cdot (\bar{\rho}\tilde{h}\tilde{\mathbf{u}}) = \frac{\partial \bar{P}}{\partial t} + \tilde{\mathbf{u}} \cdot \nabla \bar{P} + \nabla \cdot ((\lambda + \lambda_t)\nabla \tilde{T}) + \mathbf{t} \cdot \nabla \tilde{\mathbf{u}} \,. \tag{2.3}$$

$\tilde{h}$ is the sensible enthalpy defined by:

$$\tilde{h} = \int_{T_0}^{\tilde{T}} C_p dT \,. \tag{2.4}$$

The state equation for a perfect-gas mixture is:

$$\bar{P} = \bar{\rho} r \tilde{T} \,. \tag{2.5}$$

The sound speed c is defined by:

$$c^2 = \left. \frac{\partial \bar{P}}{\partial \bar{\rho}} \right|_{\tilde{T}=\tilde{T}_0} = \gamma r \tilde{T} \,. \tag{2.6}$$

The pressure dependence in the enthalpy equation (2.3) can be removed using the state equation (2.5):

$$\bar{\rho}\partial\tilde{h} = \bar{\rho} C_p \partial \tilde{T} = \frac{\gamma}{\gamma - 1} \left(\partial \bar{P} - \frac{c^2}{\gamma} \partial \bar{\rho} \right) , \tag{2.7}$$

and

$$\frac{\partial \bar{\rho}\tilde{h}}{\partial t} + \nabla \cdot (\bar{\rho}\tilde{h}\tilde{\mathbf{u}}) = -c^2\bar{\rho}\nabla \cdot \tilde{\mathbf{u}} + \gamma\nabla \cdot ((\lambda + \lambda_t)\nabla\tilde{T}) + \gamma\mathbf{t} \cdot \nabla\tilde{\mathbf{u}}\,. \tag{2.8}$$

Using (2.3) and (2.7), a similar equation for the pressure can be obtained:

$$\frac{\partial \bar{P}}{\partial t} + \tilde{\mathbf{u}} \cdot \nabla\bar{P} = -c^2\bar{\rho}\nabla \cdot \tilde{\mathbf{u}} + (\gamma - 1)\nabla \cdot ((\lambda + \lambda_t)\nabla\tilde{T}) + (\gamma - 1)\mathbf{t} \cdot \nabla\tilde{\mathbf{u}}\,. \tag{2.9}$$

2.2. *Fractional-step method*

The proposed fractional-step method is based on the splitting of the eigenvalues of the 1D compressible Navier-Stokes equations:

$$\begin{pmatrix} u + c \\ u - c \\ u \end{pmatrix} = \begin{pmatrix} u \\ u \\ u \end{pmatrix} + \begin{pmatrix} c \\ -c \\ 0 \end{pmatrix}\,. \tag{2.10}$$

The two first eigenvalues on the LHS are the speeds of the two acoustic waves. The third eigenvalue corresponds to the advection. This decomposition reveals a pure advection and a pure acoustic step in the RHS. The proposed method consists of applying this decomposition to the full Navier-Stokes equations as described in the following.

First step: Advection

In this first step, all variables are advected. For $\phi \in \{\rho, \rho\mathbf{u}, \rho h\}$,

$$\frac{\bar{\phi}^\star - \bar{\phi}^n}{\Delta t} + \nabla \cdot (\bar{\phi}\tilde{\mathbf{u}}) - \bar{\phi}\nabla \cdot \tilde{\mathbf{u}} = D_\phi\,, \tag{2.11}$$

where the diffusion and dissipation terms are $D_\rho = 0$, $D_{\rho\mathbf{u}} = \nabla \cdot \mathbf{t}$ and $D_{\rho h} = \gamma\nabla \cdot ((\lambda + \lambda_t)\nabla\tilde{T}) + \gamma\mathbf{t} \cdot \vec{\nabla}\tilde{\mathbf{u}}$. At the end of this step, the pressure $\bar{P}^\star$ is estimated from $\bar{\rho}^\star$ and $\tilde{h}^\star$ using the state equation (2.5).

Second step: Pressure correction

The second step is obtained by removing (2.11) from the Navier-Stokes equations (2.1), (2.2) and (2.8):

$$\frac{\bar{\rho}^{n+1} - \bar{\rho}^\star}{\Delta t} + \bar{\rho}\nabla \cdot \tilde{\mathbf{u}} = 0 \tag{2.12}$$

$$\frac{\bar{\rho}\tilde{\mathbf{u}}^{n+1} - \bar{\rho}\tilde{\mathbf{u}}^\star}{\Delta t} + \bar{\rho}\tilde{\mathbf{u}}\nabla \cdot \tilde{\mathbf{u}} = -\nabla\left(\frac{\bar{P}^n + \bar{P}^{n+1}}{2}\right) \tag{2.13}$$

$$\frac{\bar{\rho}\tilde{h}^{n+1} - \bar{\rho}\tilde{h}^\star}{\Delta t} + \bar{\rho}\tilde{h}\nabla \cdot \tilde{\mathbf{u}} = -c^2\bar{\rho}\nabla \cdot \tilde{\mathbf{u}}\,. \tag{2.14}$$

The same type of equation is also obtained for the pressure from (2.9):

$$\frac{\bar{P}^{n+1} - \bar{P}^\star}{\Delta t} = -c^2\bar{\rho}\nabla \cdot \tilde{\mathbf{u}}\,. \tag{2.15}$$

(2.15) directly relates the pressure variation in the second step to the velocity divergence. This relation can be used to express (2.12) to (2.14) as functions of the pressure variation $\delta\bar{P} = \bar{P}^{n+1} - \bar{P}^\star$:

$$\frac{\bar{\rho}^{n+1}-\bar{\rho}^{\star}}{\Delta t}-\frac{1}{c^2}\frac{\delta\bar{P}}{\Delta t}=0 \tag{2.16}$$

$$\frac{\bar{\rho}\tilde{\mathbf{u}}^{n+1}-\bar{\rho}\tilde{\mathbf{u}}^{\star}}{\Delta t}-\frac{\tilde{\mathbf{u}}}{c^2}\frac{\delta\bar{P}}{\Delta t}=-\nabla\left(\frac{\bar{P}^{n}+\bar{P}^{n+1}}{2}\right) \tag{2.17}$$

$$\frac{\bar{\rho}\tilde{h}^{n+1}-\bar{\rho}\tilde{h}^{\star}}{\Delta t}-\frac{\tilde{h}+c^2}{c^2}\frac{\delta\bar{P}}{\Delta t}=0\,. \tag{2.18}$$

Taking the divergence of (2.17) and using the continuity equation to remove the unknown velocity $\bar{\rho}\tilde{\mathbf{u}}^{n+1}$ leads to the Helmholtz equation:

$$\nabla\cdot\nabla\left(\delta\bar{P}\right)-\nabla\cdot\left(\frac{2\tilde{\mathbf{u}}}{c^2\Delta t}\delta\bar{P}\right)-\frac{4}{c^2\Delta t^2}\delta\bar{P}= -\nabla\cdot\nabla\left(\bar{P}^{\star}+\bar{P}^{n}\right)+\frac{4}{\Delta t}\left(\frac{\bar{\rho}^{\star}-\bar{\rho}^{n}}{\Delta t}+\nabla\cdot\left(\frac{\bar{\rho}\tilde{\mathbf{u}}^{\star}+\bar{\rho}\tilde{\mathbf{u}}^{n}}{2}\right)\right)\,. \tag{2.19}$$

The continuity equation used to remove the unknown velocity is

$$\frac{\bar{\rho}^{n+1}-\bar{\rho}^{n}}{\Delta t}+\nabla\cdot\left(\frac{\bar{\rho}\tilde{\mathbf{u}}^{n+1}+\bar{\rho}\tilde{\mathbf{u}}^{n}}{2}\right)\,, \tag{2.20}$$

and it ensures that the method is mass conservative.

2.3. *Full algorithm*

Step 1: Advection

(2.11) is solved implicitly using a Gauss-Seidel method with relaxation for all the conservative variables. The divergence operator is the kinetic-energy conserving operator described in Mahesh *et al.* (2004). At the end of the step, the intermediate pressure $\bar{P}^{\star}$ is computed using the state equation (2.5).

Step 2: Pressure correction

The Helmholtz equation (2.19) is solved implicitly by using a Stabilized Bi-Conjugate-Gradient (BiCGStab) linear solver. Then, the pressure variation $\delta\bar{P}$ is used in (2.16), (2.17) and (2.18) to obtain the values of the conservative variables at the end of the time-step. To avoid the pressure-velocity decoupling in the Helmholtz equation in the low-Mach limit, the technique of Ham & Iaccarino (2004) is used. It consists of staggering the momentum-correction equation (2.17) to obtain a compact Laplacian operator in the Helmholtz equation.

The quantities without time index in (2.17) and (2.18) can be set equal to the value at the begin of the time-step if no inner loop is used. This approximation does not affect the second-order temporal accuracy for the linear acoustics and for the low-Mach advection. For other cases, the second-order temporal accuracy is obtained by taking these values at the middle of the time-step and performing at least 2 inner-loop iterations.

2.4. *Analysis*

2.4.1. *Linear acoustics*

A linear acoustics analysis of the proposed method is performed. This analysis consists of adding a small perturbation to a uniform flow:

$$\bar{\phi} = \bar{\phi}_0 + \bar{\phi}_1\,,\ \text{with}\ \bar{\phi}_1 \ll \bar{\phi}_0\,. \tag{2.21}$$

The flow speed is assumed small, i.e. $\tilde{\mathbf{u}}_0 = 0$, and the viscous effects are neglected. The sound speed is also assumed constant. Introducing this decomposition in the advection step of the method (2.11) and keeping the first order terms simply gives $\bar{\phi}_1^\star = \bar{\phi}_1^n$ for all the variables $\phi \in \{\rho, \rho\mathbf{u}, \rho h, P\}$. As expected, the first step has no effect on linear acoustics if the flow speed is zero. The same analysis is then performed for the pressure-correction step using the fact that $\bar{\phi}_1^\star = \bar{\phi}_1^n$. The momentum equation (2.17) becomes:

$$\bar{\rho}_0 \frac{\tilde{\mathbf{u}}_1^{n+1} - \tilde{\mathbf{u}}_1^n}{\Delta t} + \nabla\left(\frac{\bar{P}_1^n + \bar{P}_1^{n+1}}{2}\right) = 0\,. \tag{2.22}$$

The density correction (2.16) combined with the continuity (2.20) leads to another relation between the velocity and the pressure:

$$\frac{1}{c^2}\frac{\bar{P}_1^{n+1} - \bar{P}_1^n}{\Delta t} + \bar{\rho}_0 \nabla\cdot\left(\frac{\tilde{\mathbf{u}}_1^{n+1} + \tilde{\mathbf{u}}_1^n}{2}\right)\,. \tag{2.23}$$

(2.22) and (2.23) are the classical linear acoustics relations discretized with a second-order temporal scheme. In the proposed method, a second-order central scheme is used for the spatial discretization so that the method is second-order in space and time for linear acoustics without inner loop.

2.4.2. *Low-Mach limit*

Investigating the behaviour of the algorithm in the low-Mach limit is very important, as in most practical combustion devices the Mach number $\mathrm{Ma} = \tilde{\mathbf{u}}/c$ is small and as the compressible solvers may be ill-conditioned in this limit (Guillard & Viozat 1998). If the Mach number tends to zero, the advection step of the proposed method remains the same. For the pressure-correction step, the Mach-dependence of each term in the Helmholtz equation can be analyzed. For (2.19) multiplied by the square of the cell-width Δx, this leads to:

$$\begin{aligned}\mathcal{O}(\delta\bar{P}) - \mathcal{O}(\mathrm{Ma}^2\mathrm{CFL}_{\mathrm{conv}}^{-1}\delta\bar{P}) - \mathcal{O}(\mathrm{Ma}^2\mathrm{CFL}_{\mathrm{conv}}^{-2}\delta\bar{P}) = \\ - \mathcal{O}(\bar{P}^\star + \bar{P}^n) + \mathcal{O}\left(\frac{4\Delta x^2}{\Delta t}\left(\frac{\bar{\rho}^\star - \bar{\rho}^n}{\Delta t} + \nabla\cdot\left(\frac{\bar{\rho}\tilde{\mathbf{u}}^\star + \bar{\rho}\tilde{\mathbf{u}}^n}{2}\right)\right)\right)\,,\end{aligned} \tag{2.24}$$

where $\mathrm{CFL}_{\mathrm{conv}} = \tilde{\mathbf{u}}\Delta t/\Delta x$ is the convective Courant number. In the zero-Mach limit, the second and third terms of the LHS vanish, and the Helmholtz equation becomes the well-known variable-density Poisson equation. Therefore, the proposed method tends for small Mach numbers to the classical variable-density low-Mach method. This implies that in the low-Mach limit, the method is well-posed and pressure fluctuations remain finite.

Moreover, if the density of the flow is constant, the third term on the LHS of (2.11), which is proportional to the velocity divergence, vanishes. Since a kinetic-energy conserving scheme (Mahesh *et al.* 2004) is used for the convective term, the advection step discretely conserves the kinetic-energy in the low-Mach limit.

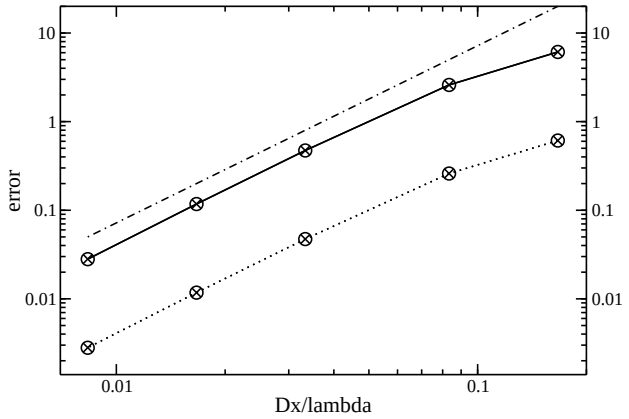

FIGURE 1. Linear acoustics. Spatial error for the pressure (multiplied by 10, solid line) and for the velocity (dotted line), without inner loop (circles) or with two iterations in the inner loop (crosses). The error is given as a function of the cell spacing divided by the wave width. The dashed-dotted line represents the second-order slope.

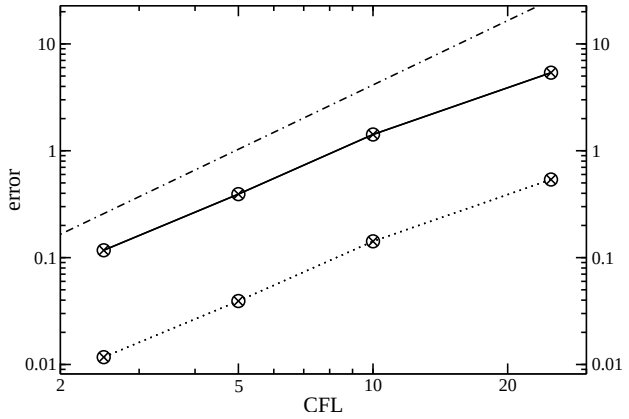

FIGURE 2. Linear acoustics. Temporal error for the pressure (multiplied by 10, solid line) and for the velocity (dotted line), without inner loop (circles) or with two iterations in the inner loop (crosses). The dashed-dotted line represents the second-order slope.

3. Results

In this section, the proposed method is verified by computing simple test cases. Then the method is applied in the computation of the cold flow of an industrial lean-premixed burner.

3.1. *Convergence-order evaluation*

3.1.1. *Linear acoustics*

A 1D Gaussian acoustic wave of small amplitude is propagated on a periodic mesh. The L2 error is computed after one acoustic time propagation. Figures 1 and 2 present the spatial and the temporal convergence of the error. The spatial error is second-order, and the temporal error is slightly less than second-order. As expected, performing two inner-loops has no effect on the error for linear acoustics.

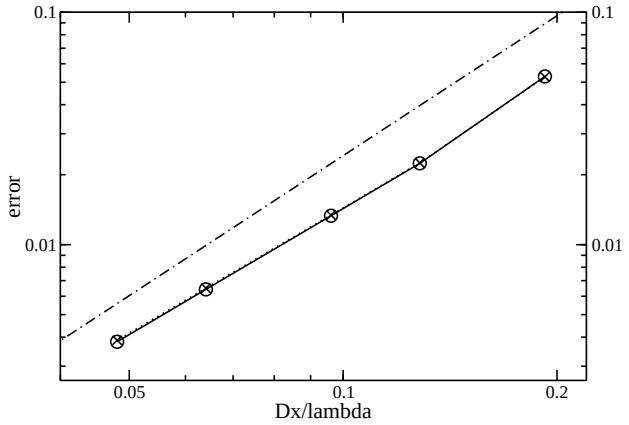

FIGURE 3. Low-Mach advection. Spatial error for the velocity without inner loop (solid line and circles) or with two iterations in the inner loop (dotted line and crosses). The error is given as a function of the cell spacing divided by the vortex width. The dashed-dotted line represents the second-order slope.

3.1.2. *Low-Mach advection*

A vortex with a low Mach number (Ma = 0.1) is propagated on a periodic mesh. Then, the L2 error is measured after one convective time. Figure 3 presents the spatial error as a function of the mesh resolution. As expected, the second-order convergence is obtained without any inner-loop.

3.2. *Unresolved homogeneous isotropic turbulence*

The case of unresolved homogeneous isotropic turbulence at infinite Reynolds number has been used by Honein & Moin (2004) to evaluate the numerical non-linear stability of different explicit methods. In the limit $\mathrm{Re} \to \infty$, the Navier-Stokes equations tend to the Euler equations, and the kinetic energy should be conserved. With the proposed method, different Homogeneous Isotropic Turbulence (HIT) computations are performed on a 32^3 Cartesian grid using the Euler equations and starting from an initially turbulent field. The turbulent Mach number of the initial field is 0.07 and the initial non-dimensionalized wave number is $k_0 = 6$. Most of the initial vortices are resolved with only five points. The kinetic-energy decay for three different acoustic CFL numbers is given in Fig. 4. For this extreme case, the computations do not blow up, and the kinetic-energy dissipation is small. For the highest CFL, 30 % of the energy is kept after ten eddy turn-over times. It must also be noted that most of the dissipation occurs after the first eddy turn-over time when the vortices are very poorly resolved on the mesh. When the vortices are better resolved, with more than four points, the dissipation is very small.

3.3. *Cold flow of a lean-premixed swirl-burner*

3.3.1. *Description*

The presented method is applied in the LES computation of the cold flow of an industrial burner (Roux *et al.* 2005). This burner features a plenum, a swirler, and a combustion chamber. A three-million hexahedral-based mesh is used. The dynamic Smagorinsky model (Germano *et al.* 1991; Lilly 1992) is used in the sub-filter closure models. Figure 5 shows instantaneous streamlines of the flow obtained with the new compressible solver. The main recirculation zones and the spreading rate of the swirling flow are clearly repre-

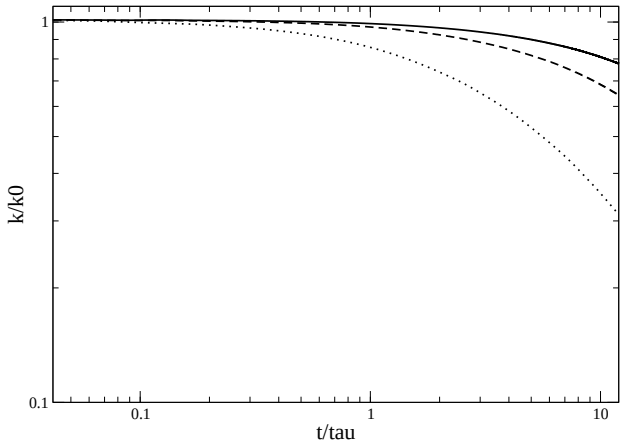

FIGURE 4. Unresolved HIT. Kinetic energy decay versus time (non-dimensionalized by the eddy turn-over time). ——— CFL=0.5, - - - - CFL=1, ····· CFL=5.

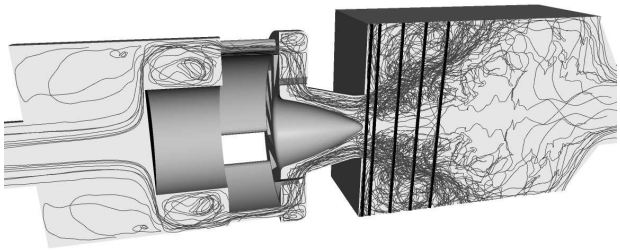

FIGURE 5. Swirl-burner. Azimuthally-projected stream-lines and velocity-data measurement locations.

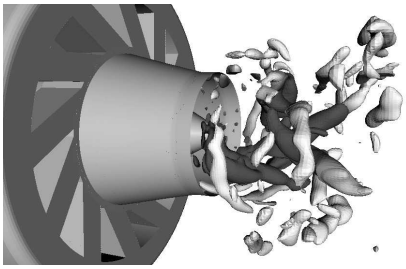

FIGURE 6. Swirl-burner. Coherent structures colored by the axis distance. The main hydrodynamic instability consists of the dark structures anchored on the injector head.

sented. The acoustic CFL number of the computation is set to a fixed value of CFL = 7. A computation with the same mean convective CFL of $\mathrm{CFL}_{\mathrm{conv}} = 0.41$ is also performed with an incompressible solver that uses the same temporal and spatial schemes. The compressible solver is only 25% more CPU expensive than the incompressible solver. This is a direct consequence of the fact that no inner loop is needed to represent correctly the main features of the flow.

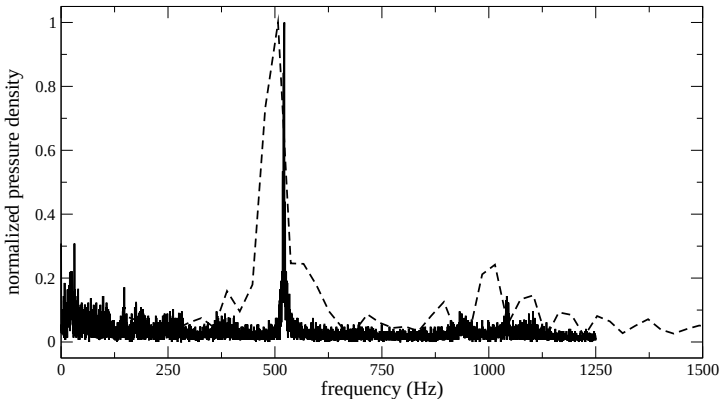

FIGURE 7. Swirl-burner. Hydrodynamic-mode frequency. ——— experiments, - - - - LES.

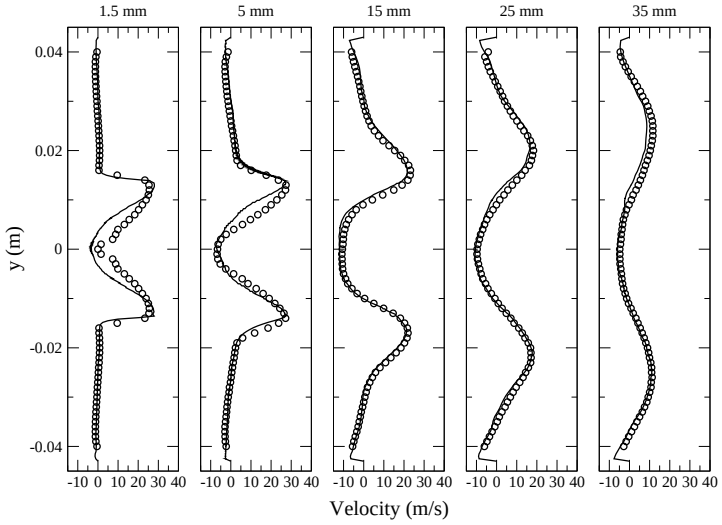

FIGURE 8. Swirl-burner. Mean axial velocity profiles. ○ experiments, ——— LES.

3.3.2. *Dynamic behavior*

Roux *et al.* (2005) have shown that the cold flow of the burner features a hydrodynamic instability. The instability they have analyzed has the structure of a Precessing Vortex Core (PVC). In the present computation, a strong hydrodynamic instability is also found, but as shown in Fig. 6, its structure is more complex. It consists of two to three interlaced vortices. The differences between the instability structures likely arise from the fact that a hexahedral-based mesh is used in this study instead of a tetrahedral-based mesh. In the LES computation, the frequency of the hydrodynamic mode is obtained by placing a pressure probe close to the injector head. The Fourier transform of the pressure signal is compared to the experimental data in Fig. 7. The computation predicts a frequency around 505 Hz close to the experimental value of 520 Hz.

3.3.3. *Velocity statistics*

Velocity statistics of LDV measurements and of the LES computation are compared in Figs. 8 to 13. The five comparison locations are given in Fig. 5. The mean and RMS

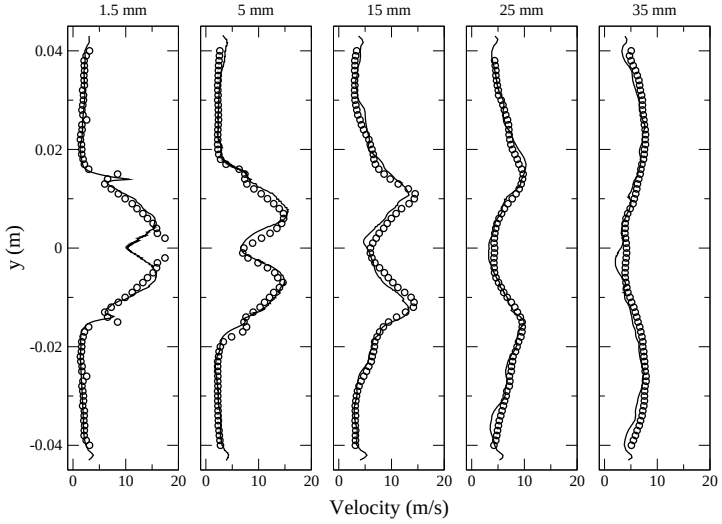

FIGURE 9. Swirl-burner. Axial velocity RMS profiles. ○ experiments, ——— LES.

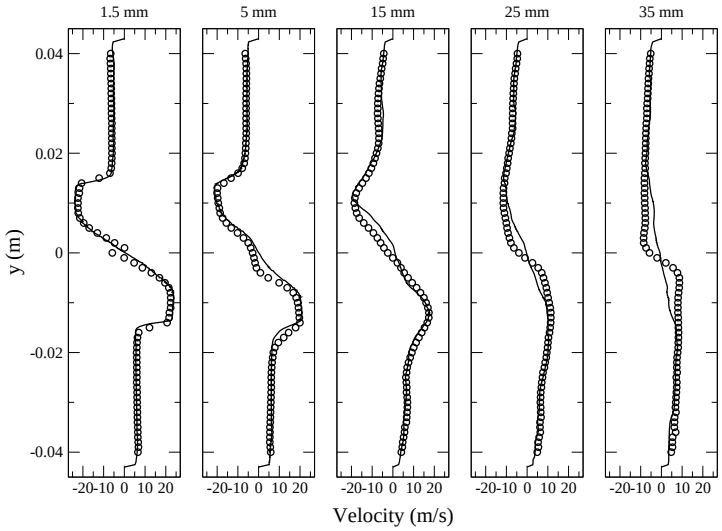

FIGURE 10. Swirl-burner. Mean azimuthal velocity profiles. ○ experiments, ——— LES.

velocities are in very good agreement for the five locations, except in a zone close to the head of the injector. This phenomenon arises from the fact that there is an uncertainty about the azimuthal position of the LDV measurements. It explains why the statistics far from the injector are in agreement while there are some differences close to the injector. It can also be noted that the LES computation cannot capture the steep gradient of the mean azimuthal velocity far from the injector. A better resolution may be needed in this region to predict this gradient.

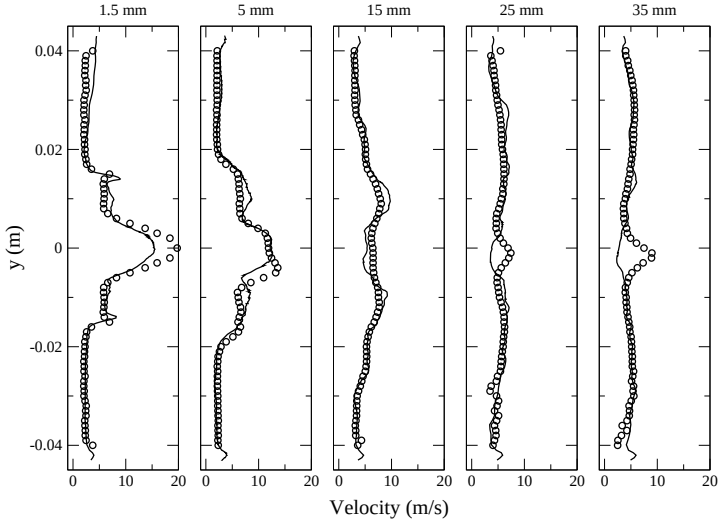

FIGURE 11. Swirl-burner. Azimuthal velocity RMS profiles. ∘ experiments, —— LES.

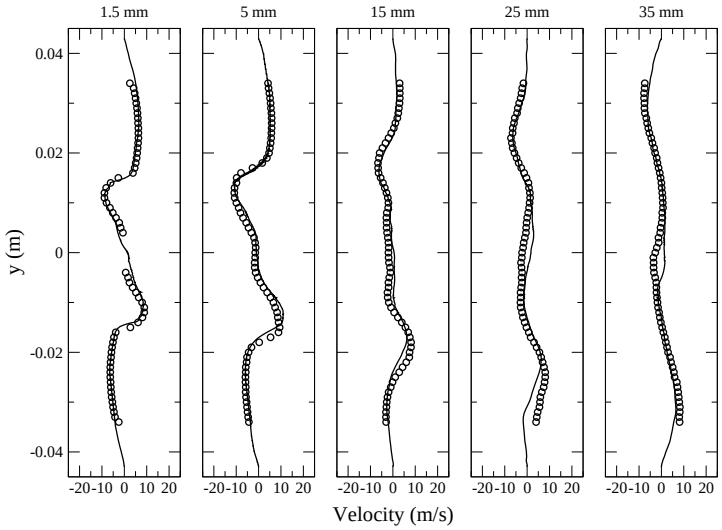

FIGURE 12. Swirl-burner. Mean radial velocity profiles. ∘ experiments, —— LES.

4. Conclusions

A new semi-implicit compressible solver for LES in complex geometries has been developed. The fractional-step method used in the solver is obtained from a characteristic splitting of the Navier-Stokes equations. This physical splitting allows for the numerical separation of the acoustics from advection. The acoustics can then be treated implicitly to remove the acoustic CFL limit. The proposed method is very efficient because it does not require inner iterations to achieve a second-order accuracy for both linear acoustics and low-Mach advection. In the low-Mach limit, the solver becomes similar to an incompressible solver, thereby inheriting the same stability and efficiency properties. A kinetic-energy conserving scheme is used for the discretization of the convective

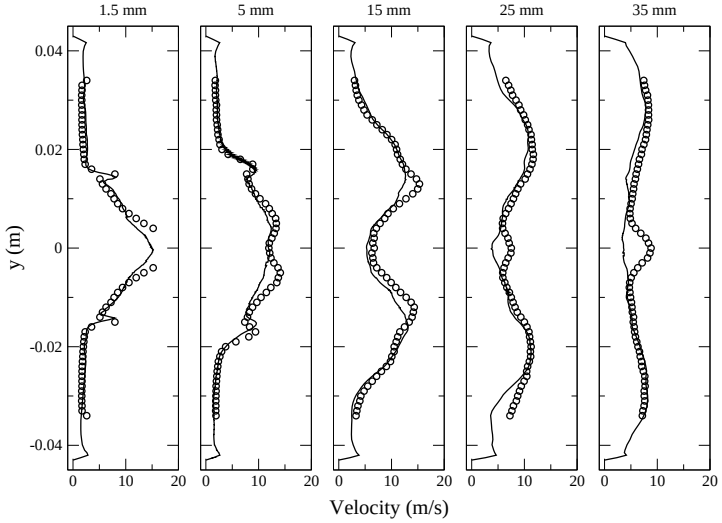

FIGURE 13. Swirl-burner. Radial velocity RMS profiles. ∘ experiments, —— LES.

terms, leading to a globally kinetic-energy conserving solver in the low-Mach limit. These properties have been illustrated and confirmed on simple test cases. The new solver has been applied in the LES computation of the cold flow of an industrial burner. The velocity statistics from the LES computation are in excellent agreement with experimental data. The dynamic behavior of the flow has also been discussed. The performance of the compressible solver has been compared to an incompressible solver featuring the same discretization schemes. The compressible solver has been found to be only 25 percent more CPU expensive than the incompressible solver, while more physics are represented. Therefore, the new solver fulfills the essential requirements for efficiency, accuracy and stability.

Acknowledgments

The authors gratefully acknowledge funding by SAFRAN Group and the US Department of Energy within the ASC program.

REFERENCES

CHOI, Y. H. & MERKLE, C. L. 1993 The application of preconditioning in viscous flows. *J. Comp. Phys.* **105**, 207–23.

GERMANO, M., PIOMELLI, U., MOIN, P. & CABOT, W. H. 1991 A dynamic subgrid-scale eddy viscosity model. *Phys. Fluids* **3**, 1760–1765.

GUILLARD, H. & VIOZAT, C. 1998 On the behaviour of upwind schemes in the low mach number limit. *Comp. Fluids* **28**, 63–86.

HAM, F. & IACCARINO, G. 2004 Energy conservation in collocated discretization schemes on unstructured meshes. *Annual Research Briefs 2004*, Center for Turbulence Research, NASA Ames/Stanford Univ., 3–14.

HARLOW, F. H. & AMSDEN, A. A. 1968 Numerical calculation of almost incompressible flow. *J. Comp. Phys.* **3**, 80–93.

Honein, A. E. & Moin, P. 2004 Higher entropy conservation and numerical stability of compressible turbulence simulations. *J. Comp. Phys.* **201**, 531–545.

Karki, K. C. & Patankar, S. V. 1989 Pressure based calculation procedure for viscous flows at all speeds in arbitrary configurations. *AIAA J.* **27**, 1167–74.

Kim, J. & Moin, P. 1985 Application of a fractional-step method to incompressible navier-stokes equations. *J. Comp. Phys.* **59**, 308–23.

Lilly, D. K. 1992 A proposed modification on the Germano subgrid-scale closure method. *Phys. Fluids* **4**, 633–635.

Mahesh, K., Constantinescu, G. & Moin, P. 2004 A numerical method for large-eddy simulation in complex geometries. *J. Comp. Phys.* **197**, 215–240.

Roux, S., Lartigue, G., Poinsot, T., Meier, U. & Berat, C. 2005 Studies of mean and unsteady flow in a swirled combustor using experiments, acoustic analysis, and large eddy simulations. *Combust. Flame.* **141**, 40–54.

Turkel, E. 1987 Preconditioned methods for solving the incompressible low speed compressible equations. *J. Comp. Phys.* **72**, 277–298.

Turkel, E., Radespiel, R. & Kroll, N. 1997 Assessment of preconditioning methods for multidimensional aerodynamics. *Comp. Fluids* **26**, 613–34.

Wall, C., Pierce, C. D. & Moin, P. 2002 A semi-implicit method for resolution of acoustic waves in low mach number flows. *J. Comp. Phys.* **181**, 545–563.

Yoon, S. Y. & Yabe, T. 1999 The unified simulation for incompressible and compressible flow by the predictor-corrector scheme based on the CIP method. *Comp. Phys. Comm.* **119**, 149–158.

Zienkiewicz, O. C., Nithiarasu, P., Codina, R., Vazquez, M. & Ortiz, P. 1999 Characteristic-based-split procedure: an efficient and accurate algorithm for fluid problems. *Int. J. Num. Meth. in Fluids* **31**, 359–92.